Experimental Thermal and Fluid Science 102 (2019) 101–112

Contents lists available at ScienceDirect

Experimental Thermal and Fluid Science

journal homepage: www.elsevier.com/locate/etfs

An experimental study on the aerodynamic performance degradation of a UAS propeller model induced by ice accretion process

Yang Liu[a], Linkai Li[a], Wenli Chen[a,b], Wei Tian[a,c], Hui Hu[a,*]

[a] Department of Aerospace Engineering, Iowa State University, 2271 Howe Hall, Room 1200, Ames, IA 50011, USA
[b] School of Civil Engr., Harbin Institute of Technology, Harbin 150090, Heilongjiang, China
[c] School of Aeronautics and Astronautics, Shanghai Jiao Tong University, Shanghai 200240, China

ARTICLE INFO

Keywords:
Unmanned Aerial System (UAS)
Propeller icing
Temporally-resolved Particle Imaging Velocimetry (PIV)
Aerodynamic degradation of UAS propeller

ABSTRACT

An experimental study was performed to investigate the effects of ice accretion on the aerodynamic performances and wake characteristics of a propeller model used for Unmanned-Aerial-System (UAS) under different icing conditions (i.e., rime *vs.* glaze). The experimental study was conducted in the unique Icing Research Tunnel available at Iowa State University (ISU-IRT). In addition to acquiring the important features of ice accretion on the rotating propeller blade using a "phase-locked" imaging technique, the wake characteristics of the rotating UAS propeller under the different icing conditions were also resolved by using the Particle Imaging Velocimetry (PIV) technique along with the time-resolved measurements of aerodynamic forces and power consumption of the UAS propeller model. Both "free-run" and "phase-locked" PIV measurements were performed on the propeller model at the different stages of the icing experiments (i.e., before, during and after the dynamic icing processes) to provide both the instantaneous flow characteristics and the ensemble-averaged flow statistics (e.g., mean velocity, vorticity, and turbulence kinetic energy) in the wake of the rotating propeller model. To the best knowledge of the authors, this is the first work of its kind to provide detailed, temporally-resolved wake flow field measurements of UAS propeller under real icing conditions. It is found that while the rime ice accretion could closely follow the original profiles of the propeller blades, the glaze ice usually forms into very irregular structures that can significantly disturb the wake flow field of the rotating propeller model, generating the much larger and more complex vortices. Such complex large-scale vortices are found to enhance the turbulent mixing in the propeller wake and produce an evident velocity deficit channel around the outer board of the propeller blades, providing direct evidences in elucidating the dramatic decrease in thrust generation and the significant increase in power consumption of the rotating propeller model in icing conditions. The findings derived from this study are believed to be essential and very helpful to elucidate the underlying mechanisms of the aerodynamic performance degradation of ice accreting UAS propellers.

1. Introduction

Ice accretion on aircraft, either unmanned or manned, has been widely recognized as a safety hazard to aviation industry. The unexpected ice accretion over in-flight aircraft surfaces has been found to not only result in a significant decrease in lift and a rapid rise in drag [1,2], but also induce unstable control conditions when ice accumulates asymmetrically on aircraft control surfaces or propulsion components [3,4]. In recent years, along with the rapid development and increased utilization of unmanned aerial systems (UASs), icing events in cold climate conditions have imposed great challenges for UAS operations [5]. Most of the UAS icing events occur when small, super-cooled, airborne water droplets freeze upon impacting the exposed surfaces of UAS, e.g., propeller blades, fixed wings, and fuselage, which allows formation of ice [6]. The freezing of the super-cooled water droplets can be complete or partial, depending on how rapidly the latent heat of fusion can be released into the ambient air [7]. If the air temperature is relatively cold (i.e., typically below $-10\,^{\circ}C$) while the liquid water content (*LWC*) is small, the impinged water droplets would freeze immediately upon impact, forming rime ice, which has an opaque appearance and conforms well with the airframe profiles. When the air temperature is just below the freezing point while the *LWC* of the airflow is relatively high, the impinged water droplets would not freeze completely upon impact due to the insufficient heat transfer to remove all of the latent heat of fusion released during the solidification process [8,9]. As a result, the unfrozen water mass would run back over the

* Corresponding author.
E-mail address: huhui@iastate.edu (H. Hu).

https://doi.org/10.1016/j.expthermflusci.2018.11.008
Received 6 September 2018; Received in revised form 13 November 2018; Accepted 18 November 2018
Available online 20 November 2018
0894-1777/

airframe surface prior to freezing downstream [7], which forms into the more transparent and complex ice shapes, i.e., glaze ice [10–12]. Due to the wet nature of glaze ice that involves complex multiphase mass and heat transfer, the formation and growth of glaze ice are more difficult to predict, due to the generation of irregular "horns" and larger "feathers" growing outward into the airflow [4]. Such large ice features were suggested to have a severe effect on the flight performance of UAS by causing large scale flow separations and unexpected structural unbalance [13,14].

In comparison with the conventional, large-sized manned aircraft, lightweight UAS is more susceptible to inflight icing events due to the lower cruising altitude, where higher humidity of air (i.e., larger *LWC*) and warmer air temperatures are more frequently forecasted. Once ice accretes on UAS surfaces, due to the limited power load of UAS, there would be a much smaller excess power margin to offset the increased drag and decreased thrust caused by ice accretion. In addition, the slower flight speed of UAS would also result in a longer duration of exposure to icing conditions, which can cause more damage to the important sensors onboard [15]. The potential damage/crash of UAS caused by in-flight icing renders their operation unfeasible in cold climates. As described in Botura and Fahrner [16], 25% of the UAS flights have encountered icing events in military actions that have negatively impacted the success of the missions. Nowadays, the most common icing avoidance strategies for UAS are to keep UAS on the ground [17] or simply modify the path planning [18], which have greatly reduced the operation capability of UAS in cold climates. This is particularly troubling for military UAS applications, in which icing conditions can lead to aborted missions and the loss of crucial tactical capabilities.

Over the years, many efforts have been made to reveal the effects of ice accretion on UAS operation capabilities. An in-flight structural icing estimation method was developed based on a 2D ice accretion prediction model [19], which evaluated the effects of airflow temperature, *LWC*, airfoil geometry, and airflow speed on the ice accretion process over UAS wings. While different scales of UAS have been developed to operate in various altitude and air velocity conditions, the effects of Reynolds number on the ice accretion process over a NACA0012 airfoil was also investigated for UAS applications, in which the regimes of *rime* and *glaze* formation as well as the ice accretion extent were identified as a function of meteorological conditions [17]. Another approach to quantify in-flight icing events is to detect the changes in aircraft performance and measurements of environmental properties, which is termed as icing-related decision-making system (IRDMS) [20]. It should be noted that, unlike most large manned aircraft which are propelled by turbo jet engines, almost all UAS are powered by propellers. Thus, when a UAS encounters an icing event, ice may accumulate not only on the fixed UAS wings, but also on the rotating blades of the UAS propeller, which can significantly degrade the flight performance of UAS due to the aerodynamic penalties of the iced propeller. However, while most of the previous studies have focused on the description of ice accretion and development of anti-/de-icing strategies on UAS wings [21,22], the dynamic ice accretion process on UAS propellers was not investigated until the recent experimental studies of Liu et al. [13,23]. In comparison to that over the surfaces of the fixed UAS wings, the dynamic ice accretion process over the rotating propeller blades was found to be much more complicated, due to the combined effects of aerodynamics forces and centrifugal forces, caused by the rotational motion of the UAS propellers. As revealed in Liu et al. [13], the ice accretion over a rotating propeller is more preferable along the radial direction, which is similar to that on wind turbine rotor blades [24,25,14]. It was also found that the ice accretion on UAS propellers, particularly in glaze icing conditions, can cause a significant reduction in thrust generation and a dramatic increase in loading fluctuating magnitude [13]. Though the effects of ice accretion on the aerodynamic performance (i.e., thrust generation and power consumption) of UAS propellers have been experimentally evaluated, the underlying mechanisms of the aerodynamic degradation of the iced UAS propellers are still not fully revealed due to the lack of knowledge of the wake characteristics of UAS propellers during the dynamic ice accretion processes.

With this in mind, we conducted an experimental study to investigate the wake characteristics of a UAS propeller model in different icing conditions (i.e., rime *vs.* glaze). The experimental study was performed in the unique Icing Research Tunnel of Iowa State University (ISU-IRT). In addition to acquiring the important features of ice accretion on the rotating propeller blade using a "phase-locked" imaging technique, the wake characteristics of the rotating UAS propeller in different icing conditions were resolved in great details by using the Particle Imaging Velocimetry (PIV) technique along with the time-resolved measurements of aerodynamic force generation and power consumption of the UAS propeller model. By correlating the wake characteristics of the ice accreting propeller model with the resultant thrust generation and power consumption during the dynamic ice accretion processes, the underlying mechanisms of the aerodynamic performance degradation of the iced UAS propeller were elucidated.

2. Test model and experimental setup

2.1. Tested UAS propeller model

The test model used in the present study is a three-blade propeller. Fig. 1 shows the schematic of the propeller model along with the typical cross section profiles of the propeller blades. The blades of the propeller have typical airfoil cross sections and platform profiles commonly used in modern propeller design. As shown schematically in Fig. 1, two airfoil profiles (i.e., ARA-D 13% and ARA-D 20%) are used at different spanwise locations along the propeller blade: while ARA-D 20% airfoil profile is used between 0.10R and 0.30R, the ARA-D 13% airfoil is used from 0.30R until the blade tip. With the prescribed blade platform profiles and twist angles (i.e., optimized based on the freestream airflow velocity and rotational speed of the propeller), a spline function is used to interpolate the prescribed cross section profiles in order to generate the three-dimensional geometry of the propeller blade. The primary design parameters of the propeller model are listed in Table 1. The propeller model is made of a hard plastic material (i.e., VeroWhitePlus, RGD835 by Stratasys, Inc.), and was manufactured by using a rapid prototyping machine (i.e., 3D printer, Connex Object 260, with accuracy of 200 μm or better). The surfaces of the propeller blades were processed with fine sandpapers (i.e., up to 2000 grit) and special plastic polishes to achieve a very smooth, glossy finish. During the experiments, an aluminum tube with a streamlined cross section was used to support the propeller model.

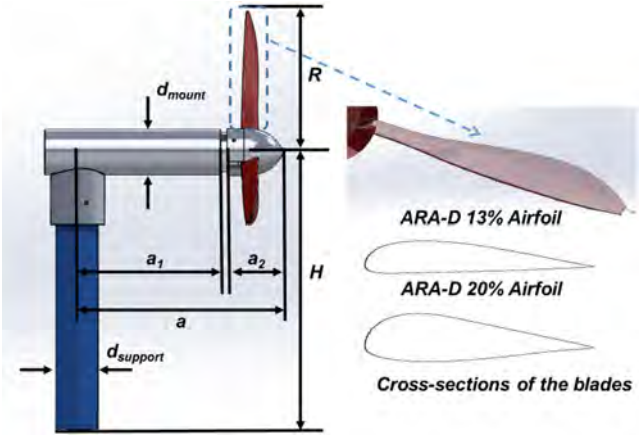

Fig. 1. Schematic of the UAS propeller model [13].

Table 1
The design parameters of the UAS propeller model.

Parameter	R (mm)	H (mm)	d_{mount} (mm)	$d_{support}$ (mm)	$a1$ (mm)	$a2$ (mm)	a (mm)
Dimension	100.00	196.10	32.20	30.00	100.96	41.00	146.86

2.2. Experimental setup

The experimental study was performed in the Icing Research Tunnel available at Aerospace Engineering Department of Iowa State University (i.e., ISU-IRT). ISU-IRT has a test section of 2.0 m in length × 0.4 m in width × 0.4 m in height with four side walls being optically transparent. ISU-IRT has a capacity of generating a maximum wind speed of 60 m/s and airflow temperature of −25 °C. An array of 8 pneumatic atomizer/spray nozzles are installed at the entrance of the contraction section to inject micro-sized water droplets (10–100 μm in size) into the airflow. By manipulating the water flow rate through the spray nozzles, the liquid water content (*LWC*) in ISU-IRT could be adjusted (i.e., *LWC* ranging from 0.1 g/m^3 to 5.0 g/m^3). In summary, ISU-IRT can be used to simulate atmospheric icing phenomena over a range of icing conditions (i.e., from dry *rime* to extremely wet *glaze* ice conditions) [26].

Fig. 2 shows the schematic of the experimental setup used in the present study. As can be seen in Fig. 2, the rotational motion of the propeller model was driven by a brushless motor (DJI 2212, 940KV), which was powered by a direct current (DC) power supply (VOLTEQ HY3050EX). During the experiments, the rotational speed of the propeller model was fixed at $n = 3000$ rpm (which corresponds to the optimum advance ratio of $J = 1.6$ at the freestream airflow velocity of $U_\infty = 16$ m/s [13]) by using a digital speed controller/manipulator to adjust the signal duty cycle of the brushless motor. In the meantime, the rotational speed of the propeller rotor was measured by a digital tachometer (MONARCH PLT200), which can generate a pulse signal from each rotation cycle of the propeller model. The tachometer-generated pulse signal was then scanned by a 16-bit data acquisition system (NI USB-6218) and sent to a digital delay/pulse generator (DDG, BNC Model-577) to trig a high-resolution imaging system for "phase-locked" image acquisition of the ice accretion process over the rotating propeller blades. A proportional-integral-derivative (PID) algorithm (i.e., a control loop feedback mechanism) was formulated to achieve automatic rotational speed correction for the propeller model as a disturbance occurs (e.g., ice accretion or ice shedding). As a result, a speed control system with feedback compensation was integrated, i.e., when a speed reduction of the propeller was detected by the digital tachometer during the ice accretion experiment, more power would be provided instantly to the motor of the propeller model to bring its rational speed back to the prescribed value. The electric currents and voltages of the DC power supply applied to the brushless motor were also recorded, which can be used to calculate the power input for the UAS propeller model during the dynamic ice accretion processes.

In the present study, a high-resolution PIV system was also used to achieve flow field measurements to quantify the complex wake structures of the propeller model during the dynamic ice accreting processes as shown in Fig. 2. For the PIV measurements before and after the ice accretion processes, the incoming airflow was seeded with ~1 μm oil droplets by using a smoke generator, while the airborne supercooled water droplets were used as the tracer particles for the PIV measurements during the ice accretion process. It should be noted that, since the supercooled water droplets suspended in the incoming airflow have a mean volume diameter (MVD) of ~20 μm, the corresponding Stokes number of the water droplets was estimated to be about 1.0, i.e., $\mathrm{Stk} = t_0 U_\infty / 2R \approx 0.1$, where $U_\infty$is the incoming airflow velocity, R is the rotational radius of the propeller, t_0 is the relaxation time of the droplet (the time constant in the exponential decay of the droplet velocity due to drag, defined as $t_0 = \rho_{water} d_{droplet}^2 / 18\mu_{air}$ where $\rho_{water}$is the density of the droplets, $d_{droplet}$is the droplet diameter and $\mu_{air}$is the dynamic viscosity of air). As suggested in Tropea and Yarin [27], particles with the Stokes number of $\mathrm{Stk} \leq 0.1$ have tracing accuracy errors of less than 1%. Therefore, the suspended water droplets are suggested to have a reasonable dynamic response to follow the incoming airflow. The illumination for the PIV measurements was provided by a double-pulsed Nd: YAG laser (i.e., New Wave, Gemini PIV 200) adjusted on the second harmonic and emitting two pulses of 200 mJ at the wavelength of 532 nm. A set of convex and concave cylindrical lenses along with optical mirrors were used to generate a laser sheet to illuminate the PIV tracers in the vertical plane passing through the symmetrical plane of the propeller model. The thickness of the laser sheet in the measurement region was set to be about 1.0 mm. A high-resolution 16-bit digital camera (2 K pixels × 2 K pixels, PCO2000, CookeCorp) was used for PIV image acquisition with the axis of the camera perpendicular to the laser sheet. The digital camera and the double-pulsed Nd: YAG laser

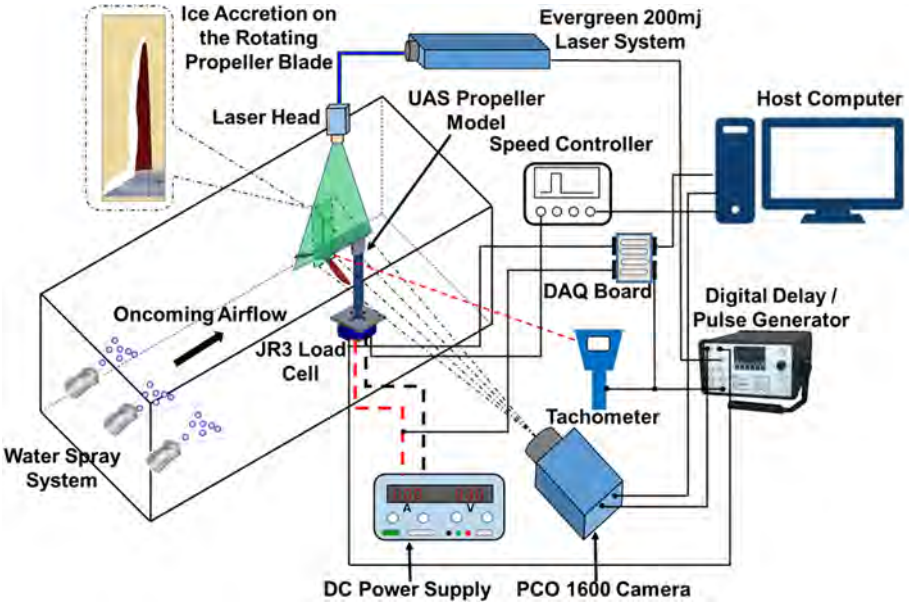

Fig. 2. A schematic of the experimental setup used in the present study.

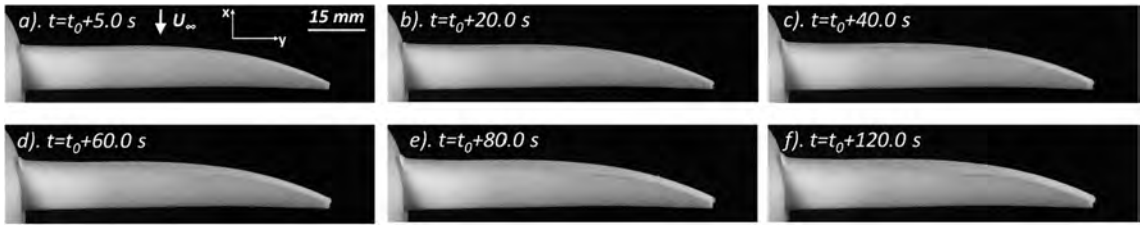

Fig. 3. Time evolution of the rime ice accretion process over the rotating propeller blade [13].

were connected to a workstation (host computer) via a digital delay generator (Berkeley Nucleonics, Model 565), which controlled the timing of the laser illumination and the image acquisition.

After PIV image acquisition, instantaneous PIV velocity vectors were obtained by a frame-to-frame cross-correlation technique involving successive frames of patterns of particle images in an interrogation window of 32×32 pixels, which has a physical area of 2.2 mm × 2.2 mm. An effective overlap of 50% of the interrogation windows was employed in PIV image processing, which results in a spatial resolution of 1.1 mm × 1.1 mm for the PIV measurements. After the instantaneous velocity vectors (u_i , v_i) were determined, the vorticity (ω_z) can be derived. The distributions of the ensemble-averaged flow quantities such as the mean velocity and in-plane turbulence kinetic energy ($\mathrm{TKE} = 0.5 \times (u'^2 + v'^2)/U_\infty^2$) were obtained from the instantaneous PIV measurements. In the present study, a cinema sequence of over 1000 frames of instantaneous PIV image pairs were obtained in order to ensure a good convergence of turbulence statistics of the PIV measurements. The measurement uncertainty level for the velocity vectors is estimated to be within 2%, while the uncertainties for the measurements of ensemble-averaged flow quantities such as turbulent kinetic energy distributions is about 5%.

In the present study, both "free-run" and "phase-locked" PIV measurements were performed on the propeller model at different stages of the icing experiments (i.e., before, during and after the dynamic icing processes) to reveal the effects of the ice accretion on the wake characteristics of the rotating UAS propeller. The "free-run" PIV measurements were conducted in order to determine the ensemble-averaged flow statistics (e.g., mean velocity, vorticity, and turbulence kinetic energy) in the propeller wake. For the "free-run" PIV measurements, the image acquisition rate was pre-selected at a frequency that is not a harmonic frequency of the rotating frequency of the propeller model in order to ensure physically meaningful measurements of the ensemble-averaged flow quantities [28]. "Phase-locked" PIV measurements were conducted to elucidate more details about the dependence of unsteady wake vortices in relation to the position of the rotating propeller blades. For the "phase-locked" PIV measurements, the digital tachometer was used to detect the position of a pre-marked propeller blade. The tachometer would generate a pulse signal as the pre-marked rotor blade passed through the vertical PIV measurement plane. The pulse signal was then used as the input signal to the DDG to trigger the digital PIV system to achieve the "phase-locked" PIV measurements. By adding different time delays between the input signal from the tachometer and the transistor-transistor logic (TTL) signal output from the DDG to trigger the digital PIV system, the "phase-locked" PIV measurements at different rotation phase angles of the pre-marked propeller blade can be accomplished [28]. At each pre-selected phase angle (i.e., corresponding to different positions of the pre-marked propeller blade related to the PIV measurement plane), more than 1000 frames of instantaneous PIV measurements were used to calculate the phase-averaged flow velocity distribution in the wake of the propeller model.

In addition to measuring the wake characteristics of the propeller model by using the PIV system, the aluminum supporting tube of the propeller model was also connected to a high-sensitivity force-moment sensor (JR3 load cell, model 30E12A-I40) to measure the dynamic aerodynamic forces generated by the propeller model. The JR3 load cell, which is composed of foil strain gage bridges, is capable of achieving time-resolved measurements of forces and the moments (torques) about each axis. The precision of the JR3 load cell for force measurements is ± 0.25% of the full range (40 N). During the experiments, the aerodynamic force data were sampled at a rate of 5000 Hz for each case.

3. Results and discussions

3.1. Dynamic ice accretion processes over the rotating UAS propeller blades under different icing conditions

As described above, a "phase-locked" imaging technique was used in the present study to provide "frozen" images of the ice features accreted on the rotating propeller blades as a function of time. Fig. 3 shows the time-evolution of the dynamic ice accretion process over one of rotating propeller blades under the test condition of freestream airflow velocity $U_\infty = 16$ m/s, $LWC = 1.0$ g/m^3, and the ambient temperature $T_\infty = -15$ °C. As can be seen clearly in Fig. 3, when the super-cooled water droplets impact on the blade surfaces under such a cold condition with low humidity, the ice accretion over the surfaces of the propeller blades exhibits typical rime characteristics (i.e., with milk-white and opaque appearances). The heat transfer process in this condition is sufficient to rapidly dissipate all the latent heat of fusion released during the solidification process of the impinged super-cooled water droplets, similar as those described in the previous studies of Hansman and Kirby [7]. As shown clearly in Fig. 3(a), since the impinged super-cooled water droplets would freeze immediately upon impact, while the accreted ice layer conforms well to the propeller blade, no surface water runback (i.e., formation of rivulet-shaped features as described in Waldman and Hu [10]) is observed over the surface of the propeller blade. As the time goes by, with more and more super-cooled water droplets impinged and frozen on the surface of the rotating propeller blade, the ice layer accreted along the leading-edge of the propeller blade is found to become thicker and thicker, as shown clearly in Fig. 3(b) to (f). It should be noted that, due to the immediate freezing of the water droplets upon impingement, no water mass runs back downstream or transport along the blade leading edge, indicating that the rime ice formation over the rotating propeller blade is not affected noticeably by the centrifugal force or the aerodynamic shear force, but principally dependent on the water collection distribution around the blade leading edge.

Fig. 4 shows the time sequence of ice accretion images of the rotating propeller blade with the freestream airflow velocity being kept the same (i.e., $U_\infty = 16$ m/s), but the LWC and the ambient temperature being increased to $LWC = 2.0$ g/m^3 and $T_\infty = -5$ °C, respectively. In comparison to the rime icing case shown in Fig. 3, much more super-cooled water droplets are impinged onto the propeller blade within the same duration of ice accretion. However, due to the relatively warm temperature of the airflow, the heat transfer process is not fast enough to remove all the latent heat of fusion released during the solidification process of the impinged super-cooled water droplets. As a result, only a portion of the super-cooled water droplets is frozen into ice upon impact, with the remaining water mass being transported freely over the surface of the propeller blade. Thus, the ice accretion over the blade

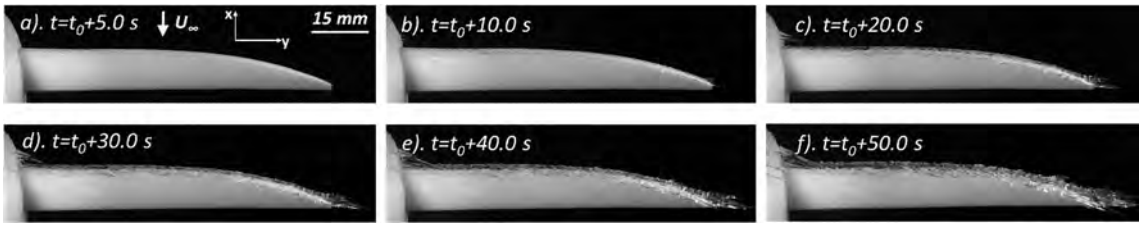

Fig. 4. Time evolution of the glaze ice accretion process over the rotating propeller blade [13].

surface in this test case is found to be a typical glaze ice accretion process. As can be seen clearly in Fig. 4, the impinged water mass is transported quickly away from the direct impingement zone (i.e., the region near the leading edge of the propeller blade) due to the combined effects of the aerodynamic force exerted by the boundary layer airflow and the centrifugal force associated with the rotation motion of the propeller. As a result, while the ice layer accreted over the surface of the propeller blade extends further downstream, the unfrozen surface water is also pushed to flow radially from the blade root to the tip due to the effects of the centrifugal force. Thus, the ice layer accreted over the outer bound of the propeller blade (i.e., in the region near the blade tip) is found to grow much faster than that at the inner bound of the propeller blade (i.e., in the region close to the blade root). Meanwhile, due to the strong effects of the centrifugal force, a portion of the surface water mass is found to separate from the ice accreting blade surface and form into the icicle structures extruding outward into the airflow, as shown in Fig. 4(c). As more and more super-cooled water droplets impinged onto the propeller blade, the ice accretion process over the blade surface becomes even more complex, forming the irregular "lobster-tail-like" ice structures as shown in Fig. 4(d) to (f).

3.2. Thrust generation and power consumption of the propeller model during the dynamic icing processes

As described above, a high-sensitive JR3 load cell (Model 30E12A-I40) was also used in the present study to achieve time-resolved measurements of aerodynamic forces acting on the propeller model under different icing conditions. While similar features can also be revealed by other components of the aerodynamic forces and moments, only the measured thrust fore data are given in the present study for analysis for conciseness. In the present study, the aerodynamic force measurements were first sampled for 15 s before switching on the water spray system to start the ice accretion process, which will be used as the baseline to evaluate the effects of ice accretion on the thrust generation characteristics of the UAS propeller. Then, the aerodynamic force data were acquired continuously for about 120 s with the water spray system being switched on to enable ice accreting dynamically over the rotating propeller blades. Fig. 5 shows the measured thrust force data during the rime and glaze ice accretion, in term of the instantaneous thrust coefficient (i.e., $C_T = T/(\rho n^2 D^4)$ where n is rotational speed of the propeller, D is the diameter of the propeller, ρ is the air density, and T is thrust force generated by the propeller), normalized by the thrust coefficient before ice accretion.

As clearly shown in Fig. 5, for the rime ice accretion case (i.e., indicated by the black solid line), the measured thrust coefficient data (Gaussian-filtered mean thrust coefficient) is found to increase slightly as the ice started to accrete over the rotating propeller blades. Since the accreted ice layer in this case closely follows the original airfoil profiles of the propeller blades as shown in Fig. 3, the ice accretion actually effectively extended the chord length of the propeller blades, which can give rise to a greater lift force of the propeller blades. Therefore, the slight increase of the thrust coefficient is suggested to be caused by the increased effective chord length of the iced propeller blades and the well-preserved wake flow field of the ice accreting propeller.

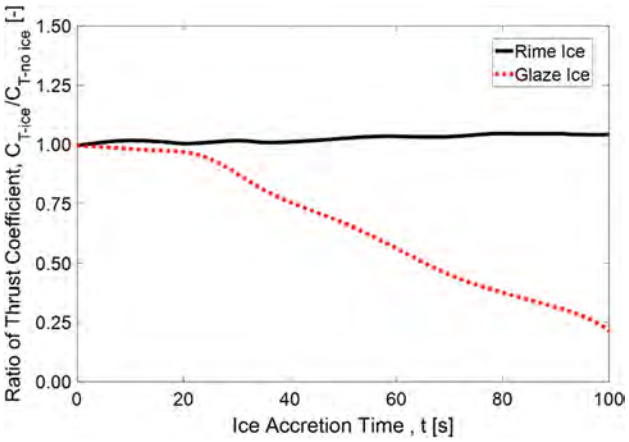

Fig. 5. Measured thrust coefficient of the propeller model during the rime and glaze ice accretion processes.

For the glaze ice accretion case (as indicated by the red[1] dotted line in Fig. 5), however, the thrust force generated by the propeller model decreases significantly (i.e., more than 75% decrease after 100 s of ice accretion). In the early stage of the glaze ice accretion, i.e., $t \leq t_0 + 20$ s, since the ice features are relatively small, the thrust coefficient of the ice accreting propeller model is almost not changed. As the time goes by, i.e., $t > t_0 + 20$ s, along with the quick growth of the irregular ice structures along the surfaces of the rotating propeller blades, the thrust coefficient of the ice accreting propeller model decreases rapidly as shown in Fig. 5. It is also suggested that due to the formation of the "lobster-tail-like" icicles over the surfaces of the propeller blades, the lift generated by the ice accreting blades is significantly reduced, which also contributed to the thrust degradation of the ice accreting propeller model.

In addition to the measuring the aerodynamic forces acting on the propeller model, the power inputs required to drive the propeller model to rotate at a constant rotation speed (i.e., $n = 3000$ rpm) under different icing conditions were also monitored in the present study. Fig. 6 shows the required power inputs to drive the propeller model during the dynamic ice accretion process under the rime and glaze icing conditions. Following the work of Brandt and Selig [29], the input power coefficient of the propeller model is defined as: $C_P = P/(\rho n^3 D^5)$ where P is the input power of the rotating propeller model. The required power inputs under different icing conditions were normalized by their corresponding baseline values without any ice accretion over the propeller blades, i.e., $Cp_{ice}/Cp_{no\text{-}ice}$, for quantitative comparison.

It is clearly seen that, for the test case with rime ice accretion over the propeller blades (as indicated by the black solid-line given in Fig. 6), the required power input increases slightly as ice begins to build up on the surfaces of the rotating propeller blades. As mentioned above, the rime ice accretion conforms well to the original profiles of the propeller blades. The slight increase of the required power input is suggested to be caused by the increase of the total mass of the ice

[1] For interpretation of color in Figs. 5, 6, and 9, the reader is referred to the web version of this article.

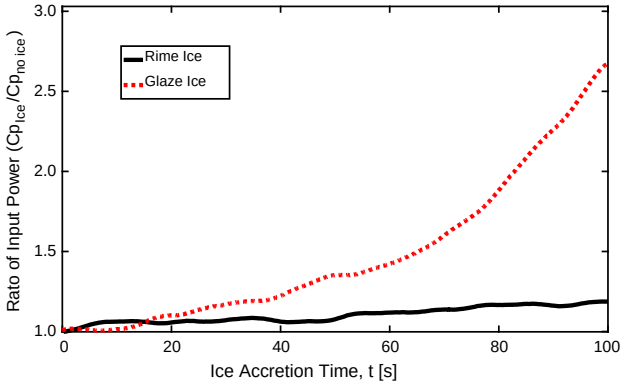

Fig. 6. The required power inputs to drive the propeller model under different icing conditions.

accreting propeller model.

For the glaze ice accretion case, however, the required power input increases dramatically (as indicated by the red dotted-line given in Fig. 6) during the dynamic ice accretion process in order to keep the propeller model at the constant rotational speed of $n = 3000$ rpm. As described above, very complex ice structures are found to be generated over the surfaces of rotating propeller blades (e.g., the formation of "lobster-tail-like" icicle structures as shown in Fig. 4). As a result, the aerodynamic drag acting on the propeller and the total mass of the rotating propeller would increase significantly, in comparison to those of the propeller model with rime ice accretion. Therefore, a much greater power input was required to keep the propeller rotating at the same rotation speed (i.e., up to about 250% more power input is required at 100 s after starting the glaze ice accretion process, as shown in Fig. 6).

3.3. Instantaneous PIV measurements to quantify the transient wake characteristics of the UAS propeller model during the dynamic icing processes

The above results have demonstrated that while the rime ice accretion has a minimum effect on the propeller performance, the very complex glaze ice structures could significantly decrease thrust generation and increase power consumption of the propeller model. In order to elucidate the underlying mechanisms of the performance degradation of the UAS propeller model under the different icing conditions, instantaneous PIV measurements were conducted in the present study to provide the very valuable transient details of the wake flow field of the ice accreting propeller model. To clearly present the transient wake evolution of the propeller model during the dynamic icing processes, the instantaneous PIV measurements were performed at a certain phase angle of the propeller rotation (i.e., 60° relative to the vertical PIV measurement plane).

Fig. 7 shows the instantaneous PIV measurements of the wake flow field of the ice accreting propeller model under the rime icing condition ($U_\infty = 16$ m/s, $LWC = 1.0$ g/m^3, and $T_\infty = -15$ °C). It is clearly seen that the transient wake flow field of the ice accreting propeller model is only changed slightly during the ice accretion process. At the beginning of the icing process, $t = t_0 + 5$ s, since there is only a very thin ice layer accreting along the propeller blades, the wake flow field is almost not disturbed as indicated in Fig. 7(a). The vortices observed in Fig. 7(d), as highlighted in the dashed ellipse, are mainly the root and mid-span vortices shedding from the original profile of the rotating propeller blades. As the time goes by, i.e., from $t = t_0 + 60$ s to $t = t_0 + 120$ s, the ice layers along the propeller blades are found to become thicker and thicker, but still follow the original profile of the blades. The wake structures of the rotating propeller is found to be changed slightly as shown in Fig. 7(b) to (c), with the tip vortices increasing slowly as highlighted in Fig. 7(e) and (f). The very small change of the wake flow field of the propeller model under the rime icing condition correlates well with the relatively small degradation of the propeller performance under such conditions.

Fig. 8 shows the instantaneous PIV measurements of wake flow field of the ice accreting propeller model under the glaze icing condition ($U_\infty = 16$ m/s, $LWC = 2.0$ g/m^3, and $T_\infty = -5$ °C). At the early stage of the icing process, due to the very small amount of ice accretion along the propeller blades, the wake structures are mainly generated from the original profile of the rotating propeller blades, with only small vortices being observed as shown in Fig. 8(a) and (d). As the time goes by, i.e., $t = t_0 + 30$ s, the ice layers along the blades are found to become thicker as more super-cooled water droplets impinged on the rotating propeller blades, resulting in the increase of the vortices in the wake flow field as shown in Fig. 8(b) and (e). Due to the wet nature of the glaze ice accretion, very irregular ice shapes are found to be formed along the propeller blades, during which process the wake flow field of the rotating propeller is found to be distorted greatly as clearly shown in Fig. 8(c). The rotating propeller with the large ice structures produces a wake flow field with much larger and more complex vortex structures as shown in Fig. 8(f). The larger vortex structures in the wake flow field essentially cause the rapid increase of drag force and greater structural vibrations. In the meantime, it is found that the width of the propeller wake is expanded quickly along with the generation of these vortices, which could induce extensive flow disturbances of the other UAS components in the wake of propeller. The temporally-resolved wake flow structures of the propeller model under the glaze ice accretion condition suggest that, the much larger irregular ice shapes formed in such wet icing conditions could dramatically contaminate the propeller wake flow field, which accounts for the significant degradation of the propeller performance (i.e., a dramatic increase in drag and a significant decrease in thrust generation).

3.4. Ensemble-averaged flow statistics in the wake flow field of the iced UAS propeller model

To further evaluate the effects of ice accretion on the wake characteristics of the rotating UAS propeller model, "free-run" PIV measurements were also conducted in the present study to determine the ensemble-averaged flow statistics (e.g., mean velocity and vorticity, turbulence kinetic energy) in the wake of the rotating propeller model under different test conditions (i.e., clean propeller model without any ice accretion, propeller model with rime ice accretion, and propeller model with glaze ice accretion). Fig. 9 shows the "free-run" PIV measurements in terms of ensemble-averaged flow velocity distributions, vorticity distributions, and the normalized in-plane Turbulence Kinetic Energy ($TKE = 0.5 \times (u'^2 + v'^2)/U_\infty^2$) distributions in the wake of the rotating propeller model under the different test conditions.

For the clean propeller model, it can be found that, as the incoming airflow passed through the rotating propeller, the velocity of the airflow is obviously increased as shown in Fig. 9(A-a). Since the propeller model is kept rotating at a constant speed of $n = 3000$ rpm by using an electrical motor, kinetic energy is continuously generated (i.e., converted from the continuous electrical energy input), which contributes to the acceleration of the airflow in the wake of the rotating propeller model. Along with the flow acceleration, alternating positive and negative vortex channels are observed in the contour of the ensemble-averaged vorticity distribution as shown in Fig. 9(A-b). These vortex channels are essentially generated due to the flow separation as the airflow passing through the rotating propeller blades, which include root vortex, mid-span vortex, and tip vortex as indicated by the alternating faint blue and red regions in Fig. 9(A-b). Though the alternating vortex structures are generated in the wake of the rotating propeller, the TKE in the wake flow field is found to be relatively small as indicated in the contour of TKE distribution in Fig. 9(A-c), i.e., the normalized TKE is smaller than 0.01 in the near wake of the rotating

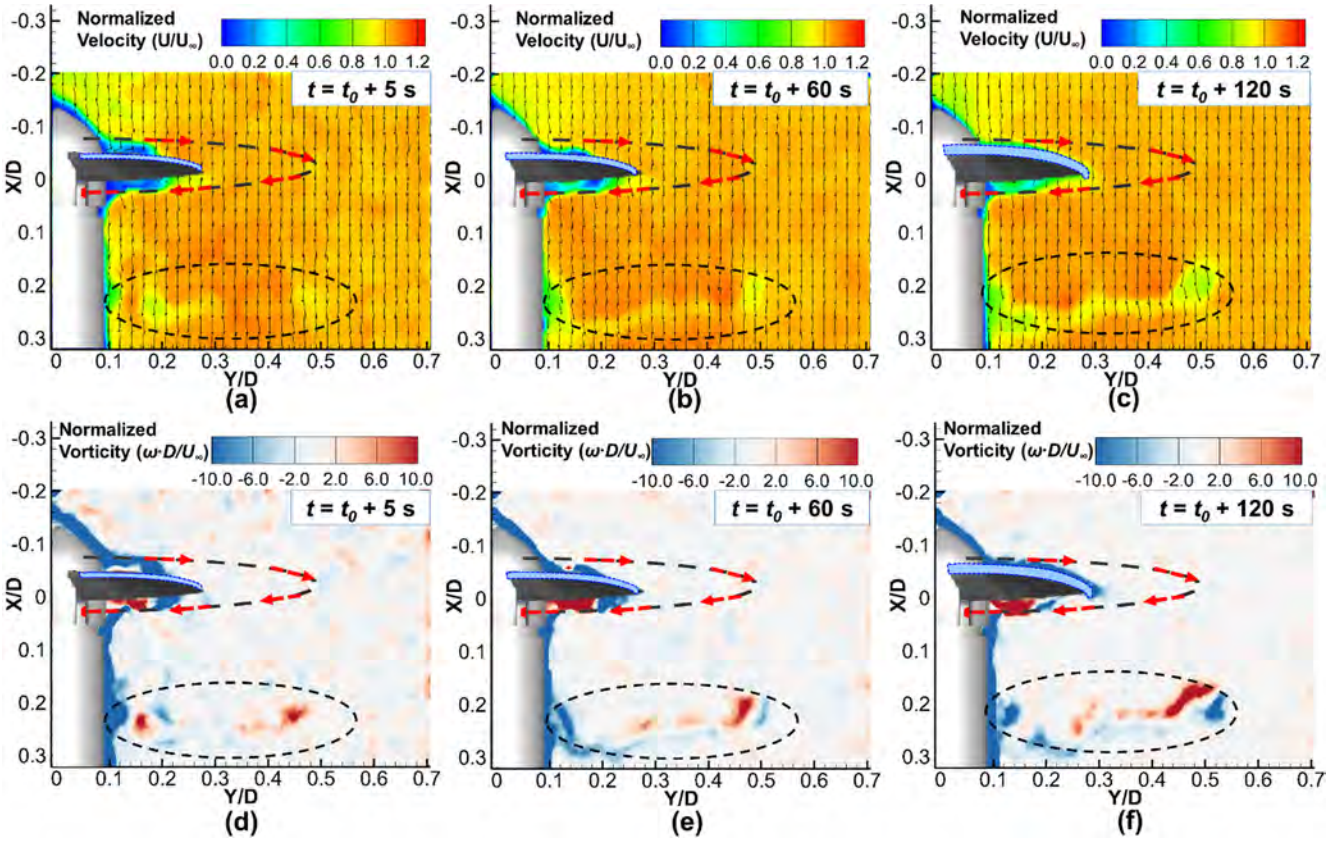

Fig. 7. Instantaneous PIV measurements of wake flow field of the ice accreting propeller model under the rime icing condition (U_∞ = 16 m/s, LWC = 1.0 g/m^3, and T_∞ = −15 °C).

propeller. Therefore, the airflow in the propeller wake is considered to be rather smooth with only the well-organized small vortices.

When rime ice accreted over the blade surfaces of the rotating propeller model, the airflow passing through the iced propeller is found to be accelerated as shown in Fig. 9(B-a), with almost the same ensemble-averaged velocity distribution as that for the clean propeller model. As described above, the ice layers formed in the rime icing condition are found to closely follow the original profile of the propeller blades, therefore, have a minimum effect on the airflow over the surfaces of the rotating blades. Such streamlined ice layers are also suggested to effectively extend the chord length and increase the thickness of the propeller blades, which can induce a slightly higher vorticity distribution in the wake flow field, especially around the outer bound region, as clearly shown in Fig. 9(B-b). Due to the very small disturbance of the rime ice formation to the airflow field, the TKE in the propeller wake is found to be almost in the same level with that of the clean propeller model as shown in Fig. 9(B-c). It should be noted that the high TKE values very near the rotating blades are caused by the local roughness disturbances of the accreted ice layer along the blade surfaces [13], which are found to be dissipated quickly within a very short distance, i.e., $X/D < 0.1$.

For the case of glaze ice accretion, due to the formation of the very complex ice structures along the propeller blades, the ensemble-averaged velocity distribution in the propeller wake is found to be significantly disturbed, with the distinct high velocity zone (in the range of $0.20 < Y/D < 0.45$) and low velocity zone (in the range of $0.45 < Y/D < 0.60$) being formed as shown in Fig. 9(C-a). When the large ice features formed over the blade surfaces, the airflow passing through the rotating blades is significantly disturbed along with the large-scale flow separations caused by the irregular ice structures. Therefore, very complex vortex structures are generated in the wake of the rotating propeller, especially near the outer bound of the propeller blades as clearly shown in Fig. 9(C-b). As the large-scale vortex structures are transported downstream, due to the turbulent mixing together with the expansion of the vortices, while the wake flow field becomes highly disordered, an evident velocity deficit channel is also found to be formed around Y/D = 0.50 as clearly shown in Fig. 9(C-a). Meanwhile, the TKE distribution in the propeller wake is also found to be increased significantly along with the transport, expanding, and mixing of the complex vortex structures as shown in Fig. 9(C-c). These significantly disturbed wake characteristics are suggested to be the direct evidence to account for the dramatic performance degradation of the propeller model under glaze icing conditions.

To quantitatively compare the wake characteristics of the rotating propeller model with the different ice accretions (i.e., rime *vs.* glaze), the transverse profiles of the mean flow velocity were also extracted from the PIV measurement results at the downstream locations of X/D = 0.15 and X/D = 0.30, respectively, as given in Fig. 10. In comparison with the velocity profiles behind a wind turbine model [28], in which obvious velocity deficits were observed in the turbine wake flow due to the harvesting of the kinetic energy in the incoming airflow by the wind turbine, the velocity profiles in the wake of the UAS propeller model showed opposite mechanisms with the airflow velocity being accelerated due to the continuous production of kinetic energy by the rotating propeller model.

Fig. 10(a) shows the velocity profiles at the downstream location of X/D = 0.15 in the wake of the propeller model under different test conditions (i.e., clean model, rime, and glaze). At such a close distance, the airflow velocity in the wake of the rotating propeller model is found to be increased in the sweeping region of the rotating propeller (i.e., $0.1 < Y/D < 0.5$). For the clean model case, the airflow velocity beyond the propeller sweeping limit, i.e., $Y/D > 0.5$, is found to quickly recover to the same level of the freestream velocity. For the case of the rime-iced propeller, since the accreted ice layers along the propeller

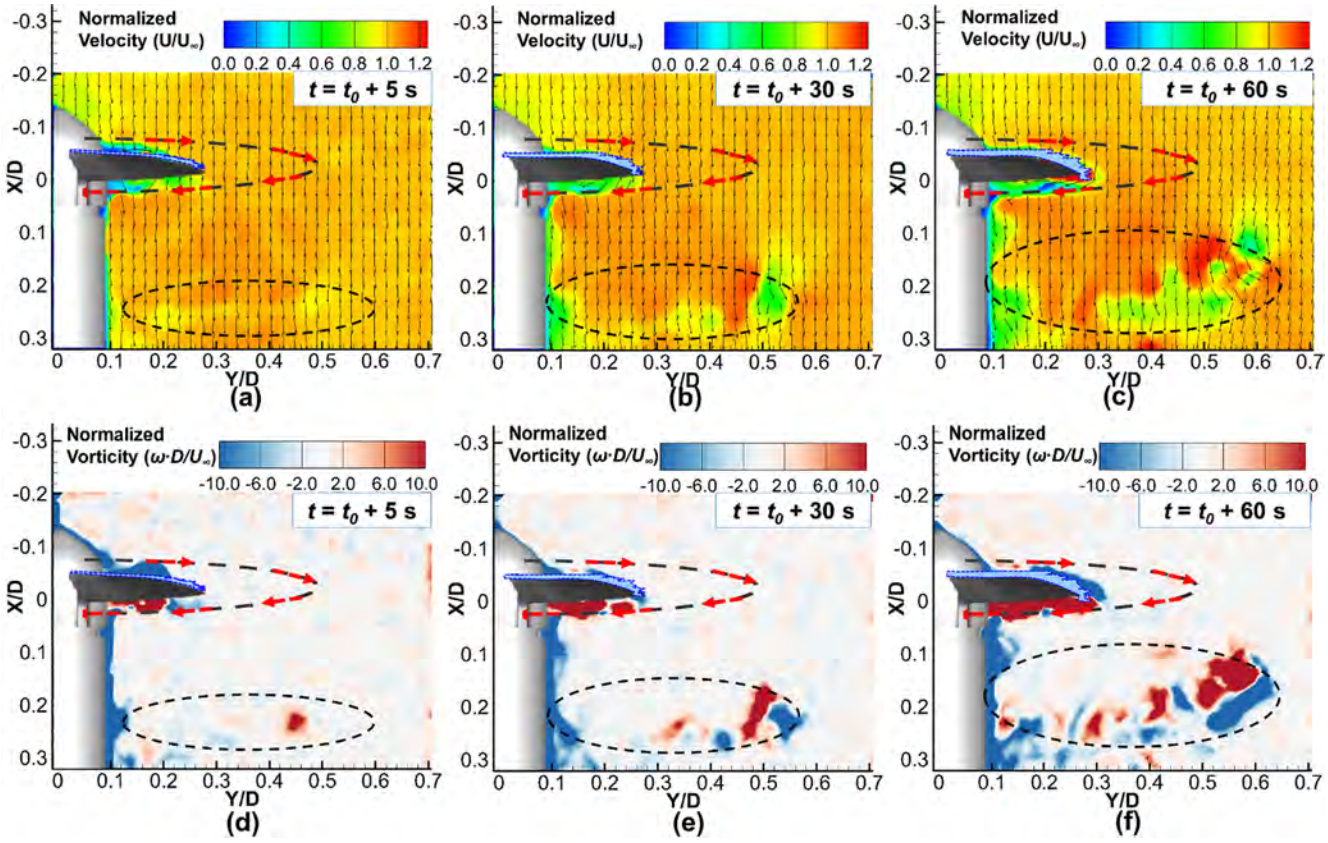

Fig. 8. Instantaneous PIV measurements of wake flow field of the ice accreting propeller model under the glaze icing condition (U_∞ = 16 m/s, LWC = 2.0 g/m^3, and T_∞ = −5 °C).

blades conform well with the original profiles of the blades, the velocity profile is found to be kept almost the same with that of the clean propeller model as shown in Fig. 10(a), indicating a stable airflow acceleration in the wake of the rime-iced propeller model. Meanwhile, a slight velocity drop is observed at the outer bound of the propeller sweeping region (i.e., Y/D = 0.5), which is suggested to be caused by the enhanced tip vortex shedding induced by the accreted ice layers along the blade leading edge of the rotating propeller model. When the irregular glaze ice structures accreted over the propeller blades, the velocity profile at the same location in the wake of the iced propeller model is found to become obviously different as shown in Fig. 10(a), corresponding to the disordered velocity distribution given in Fig. 9(C-a). It should be noted that, due to the formation of the large-scale vortex structures induced by the complex ice structures over the outer bound of the propeller blades, while the velocities within the range of $0.3 < Y/D < 0.45$ are found to have a greater increase in comparison to those in the cases of clean propeller and rime-iced propeller, a dramatic drop of the velocities is also observed from Y/D = 0.45 to Y/D = 0.5, forming a velocity deficit region as clearly shown in Fig. 10(a). The velocity profiles at the further downstream location of X/D = 0.30 are given in Fig. 10(b). While the transverse velocity distributions of the clean blade and rime-iced blade cases are almost not changed, the velocity deficit region formed in the glaze-iced case is found to become wider, which is due to the expansion of the complex vortex structures along with the turbulent mixing process.

3.5. *"Phase-locked" PIV measurements of the wake flow field of the iced UAS propeller model*

As described above, the large and complex ice structures formed over the blade surfaces of the rotating propeller model in the glaze icing condition could induce the complex large-scale vortex structures and much higher TKE in the wake flow field, which contributes to the dramatic aerodynamic degradation of the propeller model in glaze icing conditions. In order to provide further details of the wake evolution characteristics of the propeller model under glaze icing condition, "phase-locked" PIV measurements are also conducted in the present study to produce "frozen" images of the unsteady vortex structures in the wake flow field of the rotating propeller model, from which the dependence of unsteady wake vortices on the rotation of the propeller blades can be revealed more clearly and quantitatively.

Fig. 11 shows the phase-averaged velocity and vorticity distributions in the wake of the clean propeller model at three different phase angles, i.e., θ = 0°, 30°, and 60°. In the present study, the phase angle, θ, is defined as the angle between the PIV measurement plane and the position of a pre-marked propeller blade. The zero phase angle, θ = 0°, is the location of the pre-marked propeller blade when it passes through the PIV measurement plane. The phase angle would increase when the pre-marked propeller blade rotated out of the vertical PIV measurement plane. As clearly shown in Fig. 11, the incoming airflow is accelerated when it passed through the rotating propeller model, and this acceleration is found to be in phase with the rotational motion of the propeller. When the phase angle is zero, i.e., θ = 0°, the pre-marked blade is right in the PIV measurement plane. The flow velocity distribution in the wake of the propeller is uniform with the freestream airflow as shown in Fig. 11(a) and (d). As the phase angle increases to θ = 30°, i.e., the pre-marked blade rotates out of the PIV measurement plane, the vortices (i.e., root vortex, mid-span vortex, and tip vortex) generated by the pre-marked blade are transported downstream in the wake flow field (i.e., at X/D = 0.13) as clearly shown in Fig. 11(b) and (e). Along with the transport of the vortices, the airflow in upstream of the vortices is found to be accelerated as shown in Fig. 11(b). As the phase angle is further increased to θ = 60°, the vortices are transported to about X/D = 0.30. It should be noted that, during the transport process

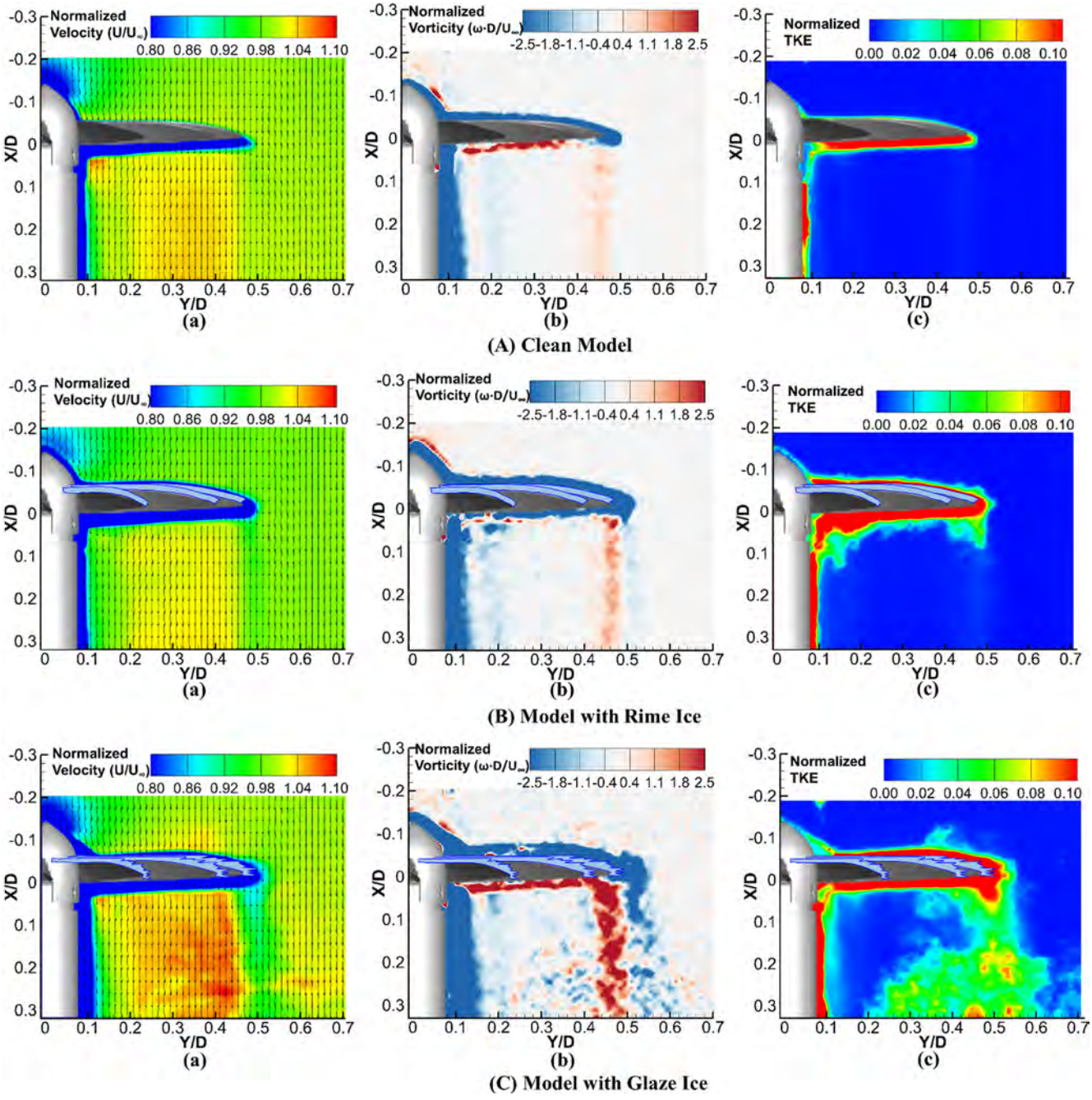

Fig. 9. Ensemble-averaged flow statistics in the wake of the rotating propeller. (A) for the clean propeller model, (B) for the propeller model with rime ice, (C) for the propeller model with glaze ice.

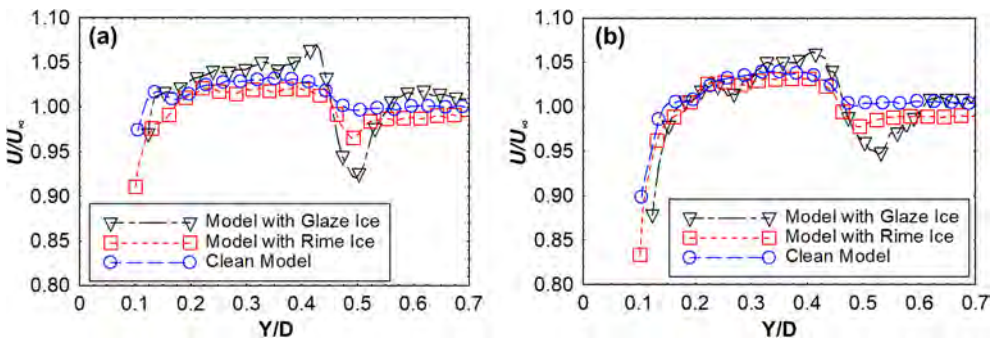

Fig. 10. Transverse velocity profiles in the wake of the rotating propeller model under different test conditions. (a) at X/D = 0.15, (b) at X/D = 0.30.

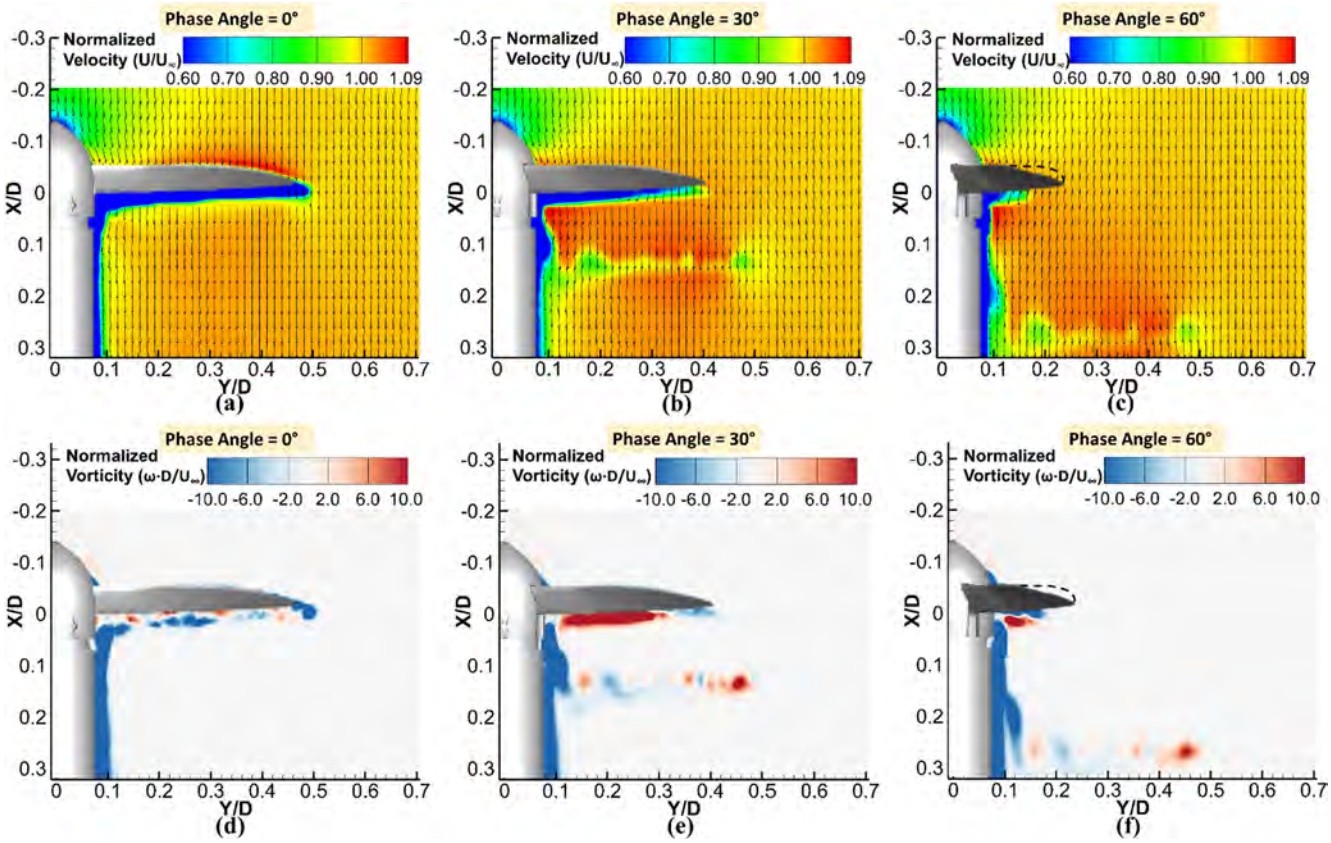

Fig. 11. "Phase-locked" flow velocity and vorticity distributions in the wake of the clean propeller model without any ice accretion.

of the vortices, the low velocity region (i.e., location of the vortices) in the wake flow field is found to be parallel with the rotational plane of the propeller.

Fig. 12 shows the phase-averaged velocity and vorticity distributions in the wake of the propeller model with glaze ice accretion at three different phase angles, i.e., $\theta = 0^{\circ}$, 30°, and 60°. In comparison to the wake characteristics of the clean propeller model, an additional pair of vortices is found to be generated at $Y/D = 0.5$, with much larger sizes and vorticities as clearly shown in Fig. 12. The additional vortices are obviously generated from the "lobster-tail-like" ice structures formed around the tip regions of the rotating propeller blades. Similar to that of the clean propeller model, the transport of the vortices as well as the flow acceleration in the wake flow field are in phase with the rotational motion of the propeller model. When the pre-marked blade passed through the PIV measurement plane, i.e., $\theta = 0^{\circ}$, the flow velocity distribution in the wake of the propeller is very uniform. However, due to the existence of the irregular ice structures around the outer bound of the propeller blade, distinct high velocity and low velocity zones are formed as clearly shown in Fig. 12(a), which is caused by the large-scale separation of the airflow behind the irregular ice shapes. As the pre-marked blade rotates out of the reference plane, i.e., $\theta = 30^{\circ}$, an evident low speed region is observed along with the transport of the vortices as shown in Fig. 12(b). It is clearly seen that the low speed region is essentially the location of the large-scale vortex structures induced by the "lobster-tail-like" ice structures as shown in Fig. 12(b) and (e). As the vortices are transported further downstream, i.e., at $\theta = 60^{\circ}$, the low speed region (where the large vortices located) is found to become larger along with the expansion and dissipation of the vortices as clearly shown in Fig. 12(c) and (f).

4. Conclusion

In the present study, a comprehensive experimental study was performed to investigate the effects of ice accretion on the wake characteristics of a UAS propeller model under different icing conditions (i.e., rime *vs.* glaze). The experimental study was conducted in the unique Icing Research Tunnel available at Iowa State University (ISU-IRT). In addition to acquiring the important features of the ice accretion on the rotating propeller blade using a "phase-locked" imaging technique, the ice-accretion-induced-wake characteristics of the rotating UAS propeller were also resolved by using a Particle Imaging Velocimetry (PIV) technique along with the time-resolved measurements of aerodynamic forces and power consumption of the UAS propeller model. Both "free-run" and "phase-locked" PIV measurements were performed on the propeller model at the different stages of the icing experiments (i.e., before, during and after the dynamic icing processes) to provide both the instantaneous flow characteristics and the ensemble-averaged flow statistics (e.g., mean velocity, vorticity, and turbulence kinetic energy) in the wake of the rotating propeller model.

Based on the "phase-locked" imaging of the dynamic ice accretion process over the blade surfaces of the rotating propeller model, it was found that while the ice layer formed in the rime icing condition would closely follow the original profiles of the propeller blades, the ice structures/shapes formed in the glaze icing condition would become very irregular with "lobster-tail-like" icicle structures accreted around the outer bound of the rotating propeller blades. By performing the instantaneous PIV measurements on the propeller model during the dynamic ice accretion processes (i.e., in both rime and glaze icing conditions), it was found that while the transient wake flow field of the ice accreting propeller model only changed slightly during the rime ice accretion process, the flow field in the propeller wake under the glaze icing condition was distorted greatly, with the generation of much larger and more complex vortex structures. Due to the dramatically different wake characteristics of the ice accreting propeller model under the different icing conditions, the measured thrust coefficient and the

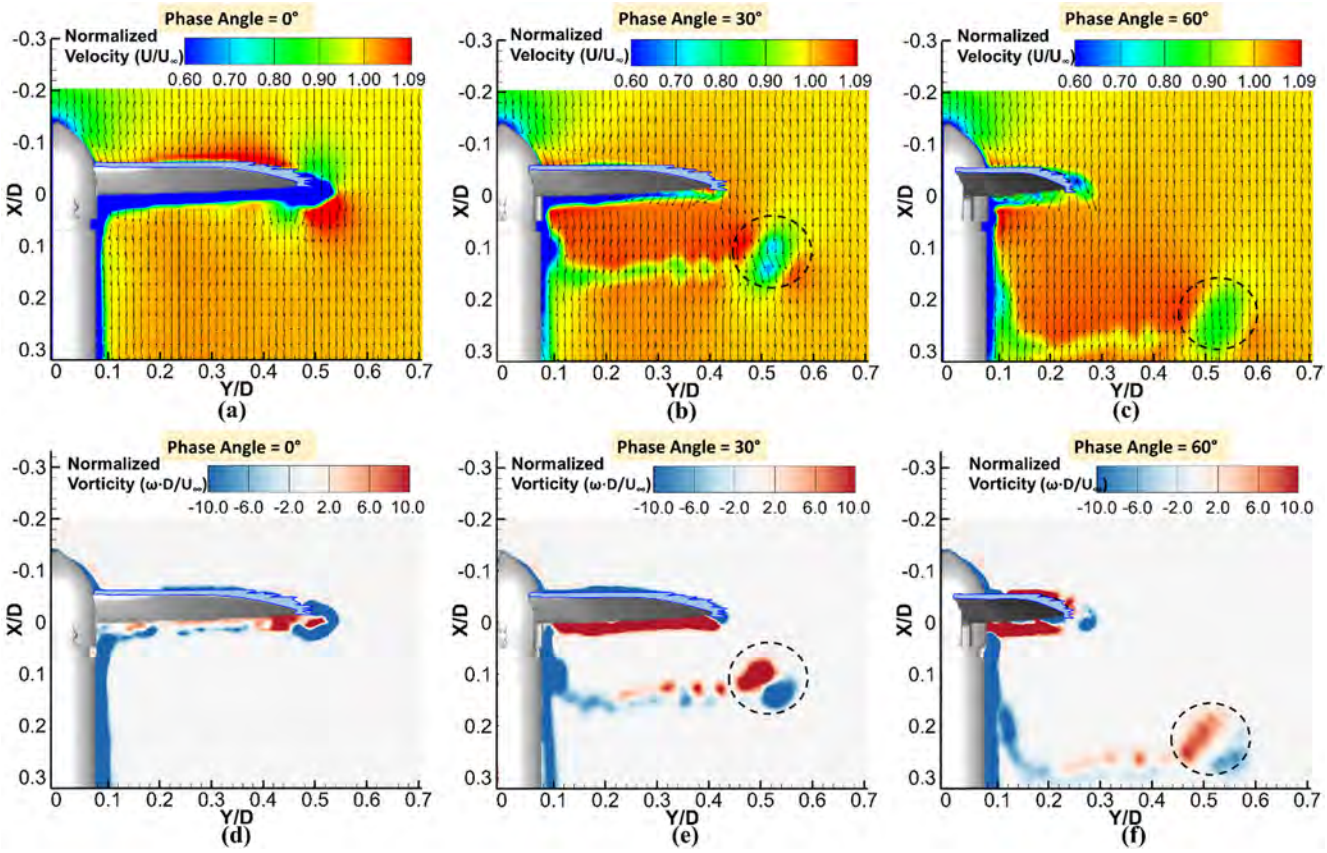

Fig. 12. "Phase-locked" flow velocity and vorticity distributions in the wake of the clean propeller model with glaze ice accretion.

power input coefficient of the rotating propeller model were also found to vary significantly under the rime and glaze icing conditions. For the rime ice accretion case, while the measured thrust coefficient data was found to increase slightly as the ice accreted over the rotating propeller blades, the required power input was also increased slightly which was mainly due to the increase of the total mass of the ice accreting propeller model. For the glaze ice accretion case, however, while the thrust force generated by the propeller model was found to decrease significantly (i.e., more than 75% decrease after 100 s of ice accretion) during the dynamic ice accretion process, the required power input was increased dramatically (i.e., up to about 250% more power input is required after 100 s of ice accretion) due to the formation of the irregular ice structures over the propeller blades.

By performing the "free-run" PIV measurements of the wake flow field of the rotating propeller model under different test conditions (i.e., clean propeller model without any ice accretion, propeller model with rime ice accretion, and propeller model with glaze ice accretion), the ensemble-averaged flow statistics (e.g., mean velocity and vorticity, turbulence kinetic energy) in the wake flow field of the propeller model were also determined in both rime and glaze icing conditions. It was found that while the airflow in the wake of the rime-iced propeller model was uniformly accelerated with only small vortices and low TKE values (which was almost the same with that of the clean propeller model), the airflow in the wake of the glaze-iced propeller model was highly disturbed with distinct high velocity zone (in the range of $0.20 < Y/D < 0.45$) and low velocity zone (in the range of $0.45 < Y/D < 0.60$) being observed, which was associated with the large-scale vortices induced by the "lobster-tail-like" ice structures. Due to the turbulent mixing together with the expansion of the large vortices, while an evident velocity deficit channel was formed around $Y/D = 0.50$, the TKE distribution in the propeller wake was also found to be increased significantly, which provided direct evidences in elucidating the dramatic decrease in thrust generation and the significant increase in power consumption of the rotating propeller model in glaze icing conditions.

In order to provide further details of the wake characteristics of the rotating propeller model in glaze icing conditions, "phase-locked" PIV measurements were also conducted in the present study to produce "frozen" images of the unsteady vortex structures in the wake flow field of the propeller model in both "clean" and "iced" conditions. It was found that there was a dependence of the unsteady wake vortices on the rotation of the propeller blades. In comparison to the wake characteristics of the clean propeller model, the wake of the glaze-iced propeller model was found to have an additional pair of vortices with much larger sizes and vorticities at the outer bound of the propeller blade, which was generated from the "lobster-tail-like" ice structures around the tip regions of the rotating propeller blades. As a result, an evident low speed region was formed together with the transport of the large vortices, which was found to become larger along with the expansion and dissipation of the vortices in the wake flow field of the rotating propeller model.

To the best knowledge of the authors, this is the first experimental study to provide detailed, temporally-resolved wake flow field measurements of UAS propeller under real icing conditions. The findings derived from this study revealed the underlying mechanisms of the aerodynamic performance degradation of ice accreting UAS propellers, which is of great importance for the modification and path design of UAS to ensure the safer UAS operations in atmospheric icing conditions.

Acknowledgments

The research work is partially supported by Iowa Space Grant Consortium (ISGC) Base Program for Aircraft Icing Studies and National Science Foundation (NSF) under award numbers of CBET- 1064196 and CBET-1435590.

References

[1] M.B. Bragg, A.P. Broeren, L.A. Blumenthal, Iced-airfoil aerodynamics, Prog. Aerosp. Sci. 41 (2005) 323–362, https://doi.org/10.1016/j.paerosci.2005.07.001.

[2] A.P. Broeren, M.B. Bragg, H.E. Addy, S. Lee, F. Moens, D. Guffond, Effect of high-fidelity ice-accretion simulations on full-scale airfoil performance, J. Aircr. 47 (2010) 240–254.

[3] J. Steuernagle, K. Roy, D. Wright, Aircraft Icing, Saf. Advis. (Weather No. 1), Air Saf. Found. Spons. by FAA, Flight Saf. Branch, 2008.

[4] S.E. Campbell, A.P. Broeren, M.B. Bragg, Sensitivity of aircraft performance to icing parameter variations, J. Aircr. 44 (2007) 1758–1760, https://doi.org/10.2514/1.32355.

[5] R.A. Hann, K. Wenz, T.A. Gryte, Johansen Impact of atmospheric icing on UAV aerodynamic performance, Work. Res. Educ. Dev. Unmanned Aer. Syst. IEEE, 2017, pp. 66–71, , https://doi.org/10.1109/RED-UAS.2017.8101645.

[6] K. Szilder, W. Yuan, In-flight icing on unmanned aerial vehicle and its aerodynamic penalties, in: D. Knight, Y. Bondar, I. Lipatov, P. Reijasse (Eds.), Prog. Flight Phys., EDP Sciences, Les Ulis, France, 2017, pp. 173–188, , https://doi.org/10.1051/eucass/2016090173.

[7] R.J. Hansman, M.S. Kirby, Comparison of wet and dry growth in artificial and flight icing conditions, J. Thermophys. Heat Transf. 1 (1987) 215–221.

[8] Y. Liu, H. Hu, An experimental investigation on the unsteady heat transfer process over an ice accreting airfoil surface, Int. J. Heat Mass Transf. 122 (2018) 707–718, https://doi.org/10.1016/j.ijheatmasstransfer.2018.02.023.

[9] K. Yamaguchi, R.J. Hansman, Heat transfer on accreting ice surfaces, J. Aircr. 29 (1992) 108–113.

[10] R.M. Waldman, H. Hu, High-speed imaging to quantify transient ice accretion process over an airfoil, J. Aircr. 53 (2015) 369–377, https://doi.org/10.2514/1.C033367.

[11] Y. Du, Y. Gui, C. Xiao, X. Yi, Investigation on heat transfer characteristics of aircraft icing including runback water, Int. J. Heat Mass Transf. 53 (2010) 3702–3707, https://doi.org/10.1016/j.ijheatmasstransfer.2010.04.021.

[12] R.J. Hansman, S.S.R. Turnock, Investigation of surface water behavior during glaze ice accretion, J. Aircr. 26 (1989) 140–147.

[13] Y. Liu, L. Li, Z. Ning, W. Tian, H. Hu, Experimental investigation on the dynamic icing process over a rotating propeller model, J. Propuls Power. (2018) 1–14, https://doi.org/10.2514/1.B36748.

[14] Y. Han, J. Palacios, S. Schmitz, Scaled ice accretion experiments on a rotating wind turbine blade, J. Wind Eng. Ind. Aerodyn. 109 (2012) 55–67, https://doi.org/10.1016/j.jweia.2012.06.001.

[15] Héloïse Beaugendre, François Morency, W.G. Habashi, FENSAP-ICE's three-dimensional in-flight ice accretion module: ICE3D, J. Aircr. 40 (2003) 239–247, https://doi.org/10.2514/2.3113.

[16] G. Botura, A. Fahrner, Icing detection system–conception, development, testing and applicability to UAVs, in: AIAA Pap. 2003-6637, San Diego, California, 2003. http://doi.org/10.2514/6.2003-6637.

[17] K. Szilder, S. McIlwain, In-flight icing of UAVs – the influence of flight speed coupled with chord size, Can. Aeronaut. Sp. J. 58 (2012) 83–94, https://doi.org/10.5589/q12-007.

[18] B. Zhang, L. Tang, M. Roemer, Probabilistic weather forecasting analysis for unmanned aerial vehicle path planning, J. Guid. Control. Dyn. 37 (2014) 309–312, https://doi.org/10.2514/1.61651.

[19] Z. Bottyán, In-flight icing characteristics of unmanned aerial vehicles during special atmospheric condition over the carpathian-basin, Acta Geogr. Debrecina. Landsc. Environ. 7 (2013) 74–80 (accessed November 24, 2016), http://search.proquest.com/openview/799d68c554353487debc7fef40749e34/1?pq-origsite=gscholar.

[20] S.F. Armanini, M. Polak, J.E. Gautrey, A. Lucas, J.F. Whidborne, Decision-making for unmanned aerial vehicle operation in icing conditions, CEAS Aeronaut. J. 7 (2016) 663–675, https://doi.org/10.1007/s13272-016-0215-2.

[21] N. Williams, A. Benmeddour, G. Brian, M. Ol, The effect of icing on small unmanned aircraft low Reynolds number airfoils, 17th Aust. Int. Aerosp. Congr. AIAC 2017, Royal Aeronautical Society, Barton, 2017, pp. 19–25.

[22] A.S. Avery, J.D. Jacob, Evaluation of low altitude icing conditions for small unmanned aircraft, 9th AIAA Atmos. Sp. Environ. Conf., American Institute of Aeronautics and Astronautics, 2017, https://doi.org/10.2514/6.2017-3929.

[23] Y. Liu, L. Li, H. Li, H. Hu, An experimental study of surface wettability effects on dynamic ice accretion process over an UAS propeller model, Aerosp. Sci. Technol. 73 (2018) 164–172, https://doi.org/10.1016/j.ast.2017.12.003.

[24] J. Palacios, E. Smith, J. Rose, R. Royer, Ultrasonic de-icing of wind-tunnel impact icing, J. Aircr. 48 (2011) 1020–1027, https://doi.org/10.2514/1.C031201.

[25] F. Lamraoui, G. Fortin, R. Benoit, J. Perron, C. Masson, Atmospheric icing impact on wind turbine production, Cold Reg. Sci. Technol. 100 (2014) 36–49, https://doi.org/10.1016/j.coldregions.2013.12.008.

[26] Y. Liu, L. Ma, W. Wang, A.K. Kota, H. Hu, An experimental study on soft PDMS materials for aircraft icing mitigation, Appl. Surf. Sci. 447 (2018) 599–609, https://doi.org/10.1016/J.APSUSC.2018.04.032.

[27] C. Tropea, A.L. Yarin, Springer Handbook of Experimental Fluid Mechanics, Springer Science & Business Media, 2007.

[28] W. Tian, A. Ozbay, H. Hu, Effects of incoming surface wind conditions on the wake characteristics and dynamic wind loads acting on a wind turbine model, Phys. Fluids. 26 (2014) 125108, https://doi.org/10.1063/1.4904375.

[29] J. Brandt, M. Selig, Propeller Performance Data at Low Reynolds Numbers, in: AIAA Pap. 2011-1255, 2011. http://doi.org/10.2514/6.2011-1255.